



# Can satellite altimetry observe coastally trapped waves on sub-monthly timescales?

Marcello Passaro<sup>1</sup>

<sup>1</sup>Deutsches Geodätisches Forschungsinstitut der Technischen Universität München, Arcisstraße 21, 80333 Munich, Germany. **Correspondence:** Marcello Passaro (marcello.passaro@tum.de)

Abstract. Coastally trapped waves (CTWs) are a major cause of sub-seasonal coastal sea level variability. While they have mostly been studied using numerical models, observational evidence is limited due to the sparse spatial coverage of the tide gauge network and the limitations of satellite altimetry gridded maps, which arise from the interpolation of sparse along-track data. The simultaneous operation of multiple altimetry missions, advancements in processing technologies, the advent of wide-swath altimetry, and the development of new interpolation techniques have the potential to significantly improve the monitoring of CTWs. In this study, we analyze three months of sea level data from satellite altimetry to evaluate the new capabilities for detecting sub-monthly variability, comparing the results to tide gauge data and an ocean model in Eastern Australia, an area known for its dominance of CTWs at these time scales. The results demonstrate that in the study area, the correlation between tide gauges and coastal daily sea level grids from satellite altimetry exceeds 0.5, even when considering time series filtered to capture only sub-monthly variability. CTWs are generally well detected, though discrepancies remain, particularly in terms of amplitude.

#### 1 Introduction

Satellite altimetry is a remote sensing technique based on the analysis of the returned signal sent from a radar, which provides the measurement of the distance between the satellite and the ocean surface (range) (Chelton et al., 2001). The range is then corrected for instrumental, atmospheric, and geophysical effects and subtracted from the orbit altitude to obtain the sea level height (Andersen and Scharroo, 2011). The data collected along the track of each satellite are then referred to a mean sea surface, cross-calibrated, and interpolated in the form of regularly spaced grids (Le Traon et al., 1998). These grids are currently released at a daily rate. Nevertheless, since they require the interpolation of scattered data in space and time, their effective resolution in time and space differs from the grid spacing and data rate (Ballarotta et al., 2019). Moreover, the effective resolution strongly depends on the number of satellites used for data collection.

Although long-term sea level variability is dominated by annual and interannual variations, it is known from in-situ data, models, and reanalysis that strong variations occur at submonthly scales, particularly in the shelf seas and coastal zones (Woodworth et al., 2019). One of the main dynamics in these regions is coastally trapped waves (CTWs), which are forced by winds and propagate the energy transmitted from the atmosphere to the ocean (Hughes et al., 2019). Although these phenomena have been reported in many regions of the world (see Aydın and Beşiktepe (2022) for a comprehensive list), a systematic





observational-based analysis is made difficult by the coarse spatial resolution of the global tide gauge network (Woodham et al., 2013).

Sea level maps from satellite altimetry could provide an excellent monitoring system for these important dynamics, but they are typically disregarded for two main reasons. First, the need for spatio-temporal interpolation and the reduced data quality in the coastal zone may affect the ability to spatially constrain the CTWs, particularly in narrow shelves. Secondly, previous literature has defined the effective temporal resolution of these maps to be about one month (Ballarotta et al., 2019), although this points more to a worsening of the signal-to-noise ratio at higher frequencies, rather than to a complete absence of a signal. As a consequence, the literature has mainly relied on models and tide-gauge data to study CTWs, while altimetry has been used only to study large-scale phenomena at temporal scales of a month or more (Poli et al., 2022; Polo et al., 2008; Kemgang Ghomsi et al., 2024).

In recent years and months, several innovations have occurred that could lead to improved capabilities in describing CTWs in altimetry maps. There have never been so many altimeters in orbit, which means that the amount of data is significantly higher than in previous years (The International Altimetry Team, 2021). The quality of the data in the coastal zone has been significantly improved by the use of new processing techniques and better geophysical corrections (Donlon et al., 2021). The successful launch of the Surface Water and Ocean Topography (SWOT) mission means that, for the first time, two-dimensional snapshots of sea level at an unprecedented spatial resolution can be combined with traditional one-dimensional along-track data (Fu et al., 2024). New interpolation algorithms have been designed to exploit the potential improvements coming from these innovations (Passaro and Juhl, 2023; Ballarotta et al., 2025; Beauchamp et al., 2023).

The objective of this work is to provide a first assessment of the capability of state-of-the-art sea level maps based on satellite altimetry to detect sub-monthly CTWs. As a testbed, the Eastern Coast of Australia was chosen. This choice is justified by the fact that the region is characterized by a narrow shelf, whose sea level variability is dominated by CTWs on timescales ranging from one day to several months (Maiwa et al., 2010). Moreover, Woodham et al. (2013) has shown that model data from the Bluelink ocean forecasting system (Schiller et al., 2019) can effectively describe the CTWs and can be validated with the local tide gauge network.

#### 50 2 Data

## 2.1 Tide Gauges

Tide gauges (TG from now on) are used in this study to compare the results obtained from other data sources. High-frequency (hourly) data, similar to those distributed by the Global Extreme Sea Level Analysis (GESLA-3, www.gesla.org, Woodworth et al. (2016)), are used. Since the GESLA-3 data available online end in 2022, a specific update was requested, and data for 2023 were obtained through personal communication with Ivan Haigh (University of Southampton, UK) and Ben Hague (Bureau of Meteorology, Australia).

Stations in Eastern Australia within the rectangle visible in Figure 1 were selected. Stations were retained if they ensured a minimum spacing of 50 km between them and were at least 25 km away from a river mouth. Based on data availabil-





ity and these criteria, the following stations were used: Bermagui, Crookhaven\_Heads, Port\_Macquarie, Coffs\_Harbour, and Brunswick\_Heads.

To make the sea level retrievals from TGs comparable to other sources of sea level data, the following steps were performed. Firstly, the TG data were detided using a 40-hour LOESS filter. Previous literature has shown this to be the most effective method for reducing tidal variance for periods shorter than two days (Saraceno et al., 2008). Subsequently, the atmospheric contribution to sea level variability was removed by applying the same correction used for altimetry data, the Dynamic Atmosphere Correction from Carrère and Lyard (2003). Finally, the hourly and sub-hourly data collected by each TG were averaged to a daily rate to match the data rate of the altimeter product.

#### 2.2 Ocean Model

The approach of (Woodham et al., 2013) is followed, which studied CTWs in the same region using data from the Bluelink ReANalysis (BRAN) experiment (referred to simply as BLUELINK in the following sections). The latest version, BRAN2020, is used, which simulates the period from 1993 to 2023 with a near-global, 10-km resolution (eddy-resolving) ocean model. Through data assimilation, the model integrates observations of temperature, salinity, and sea surface height to refine the ocean state. Details of the model and an analysis of its performance can be found in (Chamberlain et al., 2021).

## 2.3 Altimetry

The altimetry data are provided at a daily rate. The latest generation, named DT2024 and available since November 2024 in the Copernicus Marine Service (CMEMS), applies for the first time a different approach compared to the optimal interpolation adopted in previous versions (e.g., Le Traon et al. (1998); Ducet et al. (2000); Pujol et al. (2016)): the Multiscale Inversion of Ocean Surface Topography (MIOST) technique (Ubelmann et al., 2021, 2022).

MIOST solves the mapping problem by integrating all components within a reduced space and utilizing a preconditioned conjugate gradient method (Ubelmann et al., 2021). This iterative process continuously refines the solution until convergence. Once the final reduced solution is obtained, it is projected back onto the full spatial grid using wavelet-based transformations specific to each component.

The MIOST technique is also applied to an experimental product distributed by AVISO, representing the first attempt to combine traditional Level-3 along-track sea level anomalies with the two-dimensional Level-3 product from the SWOT mission (Dibarboure et al., 2025). Besides the integration of the swath-altimeter data, minor methodological differences include a different selection of the components of the wavelet-based transformations (M. Ballarotta, personal communication).

For the remainder of this paper, to distinguish between the two data sources, "CMEMS" refers to the daily grids obtained using only nadir altimeters, while "MIOST" refers to the experimental product that integrates the Level-3 product from SWOT.

Three months of data (from September 2023 to November 2023) are considered during the science phase of SWOT. In this period, both CMEMS and MIOST blend along-track measurements from the following nadir altimeters: SARAL/AltiKa, Cryosat-2, HaiYang-2B, Jason-3, Sentinel-3A, Sentinel-3B, Sentinel-6A, and SWOT nadir.





#### 3 Methods

#### 3.1 Filtering

For each latitude-longitude point of all the data sources listed above, a time series is produced and stored at a daily rate, which is referred to as unfiltered sea level. Subsequently, the time series is band-pass filtered using a Butterworth bandpass filter, filtering out components longer than 29 days (0.15 cycles per day in frequency) and shorter than 7 days (0.035 cycles per day in frequency).

#### 3.2 Lag-correlation

100

A correlation analysis is performed to study the consistency of the dataset with the ground truth represented by the TG data. The computation is based on the Pearson correlation coefficient to measure the linear relationship between time series X and Y:

$$r = \frac{\sum_{i=1}^{n} (X_i - \bar{X})(Y_i - \bar{Y})}{\sqrt{\sum_{i=1}^{n} (X_i - \bar{X})^2} \sqrt{\sum_{i=1}^{n} (Y_i - \bar{Y})^2}}$$
(1)

where  $X_i$  and  $Y_i$  are the individual sample points of the two time series,  $\bar{X}$  and  $\bar{Y}$  are the mean values of X and Y, respectively, n is the number of observations.

To observe the along-shore coherency of the CTWs at different time intervals, the lag-correlation is also computed. In this case, the correlation is computed between  $X_t$  and a time-shifted version of  $Y_t$ , denoted as  $Y_{t+\tau}$ , where  $\tau$  represents the lag (in days):

$$r(\tau) = \frac{\sum_{i=1}^{n-\tau} (X_i - \bar{X})(Y_{i+\tau} - \bar{Y}_{\tau})}{\sqrt{\sum_{i=1}^{n-\tau} (X_i - \bar{X})^2} \sqrt{\sum_{i=1}^{n-\tau} (Y_{i+\tau} - \bar{Y}_{\tau})^2}}$$
(2)

#### 3.3 Hovmöller diagrams and Phase-speed computation

The average propagation speed of the CTWs can be estimated using image processing methods applied to the Hovmöller diagrams. These diagrams are obtained by representing the temporal evolution of sea level anomalies along equally spaced points along the coastline, which are associated with the closest grid point of each dataset. The propagation speed of the observed contours is then computed based on the slopes that can be derived using image processing methods. The method based on the Radon transform, as described in De-Leon and Paldor (2017), is followed. First, the Hovmöller diagrams are normalized to the range 0–1. The Radon transform works by considering straight lines in the 2D field, which are rotated by an angle  $\theta$  and shifted by a distance s. It is defined as:





$$R_f(s,\theta) = \int_{-\infty}^{\infty} f(s\cos\theta - t\sin\theta, s\sin\theta + t\cos\theta) dt,$$
(3)

where  $R_f(s,\theta)$  is the Radon transform of f(x,y), s is the perpendicular distance of the line from the origin,  $\theta$  is the angle of the line relative to the ordinate, and t is a parameter along the line L, integrating over all points on that line. The transform sums the squares of the 2D field along each straight line to quantify the energy of the features aligned at each angle:

120 
$$E(\theta) = \int_{-\infty}^{\infty} R_f^2(s,\theta) \, ds. \tag{4}$$

The best estimate of the westward propagation speed is then the tangent of the angle at which the sum of the squares reaches its maximum:

$$v = \tan(\theta_{\text{max}}),\tag{5}$$

where v represents the westward propagation speed.

## 25 3.4 Empirical Orthogonal Functions Analyis

To determine whether the CTWs represent a dominant pattern of the sub-monthly coastal sea level variability, an Empirical Orthogonal Functions (EOF) analysis is performed on the same time series used to construct the Hovmöller diagrams, i.e. the filtered sea level along equally-spaced coastal points.

The EOF analysis is a well-known technique to identify variability patterns in time and space and has also been used for this purpose in previous studies based on CTWs. The coastal time series can be represented as a matrix X, where each row corresponds to a spatial location and each column corresponds to a time step. An anomaly matrix X' is then computed by subtracting the mean at each spatial location to remove the temporal trend. To identify the dominant spatial patterns, EOF analysis solves the eigenvalue problem:

$$Ce_k = \lambda_k e_k.$$
 (6)

where C is the covariance matrix, computed as:

$$C = \frac{1}{T}X'X'^{T}. (7)$$

where T is the number of time steps.





The eigenvectors  $e_k$  correspond to the EOF modes, which represent characteristic spatial patterns of variability. The eigenvalues  $\lambda_k$  quantify the amount of variance explained by each mode. Finally, the Principal Component (PC) time series describes how the EOF modes vary over time:

$$PC_k = e_k^T X'. (8)$$

#### 4 Results

145

150

155

160

165

## 4.1 1D-Validation against tide gauges

In Figure 2, an example of the time series from all data sources closest to one TG is presented, which can be qualitatively discussed before a quantification of the correlation is provided. The time series are shown in both their unfiltered and filtered versions. The TG clearly shows oscillations with a period of about 10 days and amplitudes of about 5 to 10 cm. The strongest oscillation is found around day 50 and corresponds to a maximum in the SLA.

The BLUELINK time series matches very well the TG data, capturing all the CTWs and showing a good match in terms of phase as well. Only the peak of the strongest event is slightly underestimated. The CMEMS data fail to capture most of the sub-monthly oscillations and underestimate the amplitude peak. The filtered data show only three crests that are comparable to the TG data. The MIOST data show much better agreement with the TG and BLUELINK, corresponding to at least five of the CTWs correctly observed, with amplitude and phase similar to the BLUELINK and TG estimations. However, events that almost superimpose cannot be correctly distinguished, as clearly seen between days 40 and 60.

To quantify the agreement, the correlation of BLUELINK, MIOST, and CMEMS against each TG for the unfiltered and filtered time series was computed and the results are reported in Figure 3. BLUELINK has the best score, showing higher agreement with the TGs at every station for both the unfiltered and filtered time series. Notably, the correlation coefficient is never lower than 0.7, and there is no strong sign of worse performance in the filtered version. This confirms the findings of Woodham et al. (2013) and allows us to use the reanalysis as a validation of the altimetry-based dataset in this study, in addition to the TGs, which have the obvious limitation of providing only point-wise time series at a limited number of locations and therefore contain limited spatial information.

In the unfiltered time series, MIOST performs significantly better than CMEMS, with a correlation coefficient never lower than 0.6. Most notably, while a drop in correlation is observed for both altimetry data sources when considering the filtered time series, a strong improvement is seen in MIOST compared to CMEMS. The correlation between the filtered MIOST and TGs is higher than 0.5 in four out of five stations, while for CMEMS the correlation exceeds 0.5 only in one station. The largest drop in correlation between unfiltered and filtered signals in the altimetry dataset occurs in Bermagui, the station closest to the shelf break, which in that region is located 30-40 km from the coast. The drop in correlation at high frequencies is therefore likely due to the influence of open ocean processes in the estimation of the coastal grid points.





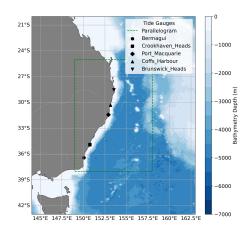


**Figure 1.** Region of study. The parallelogram shows the region in which sea level data from reanalysis and remote sensing is acquired. The tide gauge stations used in the work are also shown.

## 4.2 2D-Validation against tide gauges

175

Besides their temporal signature, we expect the sub-monthly CTWs identified in the previous section to also have a spatial signature along the shelf. The sea level oscillation caused by the CTWs can typically be observed by computing lag correlations. Moreover, Woodham et al. (2013) and our results give us confidence that the BLUELINK data can serve as a reference for the altimetry dataset. Using the filtered time series, we therefore compute the correlation coefficient between each grid point and the Bermagui TG at different lags of 0, 2, and 4 days. The results are shown in Figure 4. The same statistics have been produced for every TG station, and the corresponding figures can be found in the Appendix (Figures B1 to B4).

Taking BLUELINK as the reference, it is possible to observe how the correlation pattern is very well constrained within the shelf, which is defined by the detached line showing the bathymetric contour at -500m. The locations to the north of -31 degrees S on the shelf are anticorrelated with Bermagui at Lag 0, while the same region shows correlations well above 0.5 with a lag of 4 days. In MIOST, the same pattern as in BLUELINK can be traced, although the average correlation with the TG is generally lower than in BLUELINK, and the areas of high lag-correlation are slightly more spread outside the shelf. CMEMS also shows a similar pattern, but the level of correlation, especially at Lag 2 and Lag 4, is much lower than in MIOST and therefore less distinguishable from the random patterns in the open ocean. Observing the correlations at Lag 0, it is possible to better understand the drop in performance for Bermagui seen in Figure 3: this is due to an eddy-shaped uncorrelated feature that is not visible in the model and that MIOST and CMEMS localize on both sides of the shelf break.





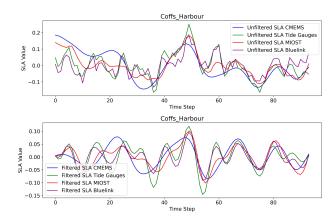


**Figure 2.** Daily sea level data from BLUELINK, CMEMS, MIOST and the Coffs\_Harbour tide gauge. The upper plot shows the full signals, while the lower plot is obtained by filtering out components longer than 29 days (0.15 cycles per day in frequency) and shorter than 7 days.

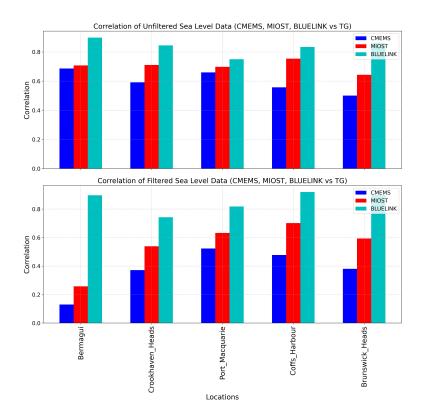


**Figure 3.** Correlation of BLUELINK, CMEMS and MIOST time series with the TG data at the closest grid point to each in-situ station. The plot shows the correlation considering unfiltered (upper panel) and filtered (lower panel) time series.





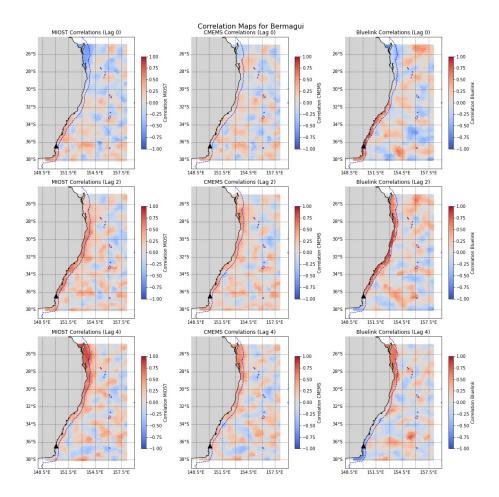


**Figure 4.** Correlation of filtered BLUELINK, CMEMS and MIOST time series at each grid point against the filtered TG data of the station Bermagui. Each row corresponds to the lag correlation at day 0, 2, 4. The bathymetry contour of -500m is shown to identify the shelf break.

# 4.3 Phase speed and EOF analysis

After subdividing the coastline into equally spaced points, we analyze the Hovmöller diagram of the filtered signals in the three datasets and compute the average phase speed of the CTWs based on the Radon transform. The results are shown in Figure 5, where the x-axis represents the distance from the southwesternmost point along the coastline. The pattern of the CTWs traveling anticlockwise along the Australian coastline is very clearly modeled by BLUELINK, but can also be recognized in MIOST and, partially, in CMEMS. The filtered altimetry time series in MIOST are good enough that it is possible to measure exactly the same phase speed of the CTWs as in BLUELINK (4.01 m/s), while the phase speed estimated for CMEMS is still very close (4.33 m/s). This is a striking result, considering that we are using the time series closest to the coastline, meaning the points for which the quality of the altimetry data is supposed to be the lowest.



200

205



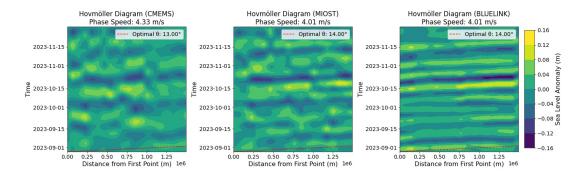


**Figure 5.** Hovmöller diagrams of CMEMS, MIOST and BLUELINK filtered time series. The point of reference of the x-axis is the southwestern most coastal point of the region of study. The dotted lines correspond to the best estimate of the westward propagation speed (see Section 3.3).

As the next step, we analyze the results of the EOF analysis applied to the filtered signal. As expected from previous studies, BLUELINK (Figure 6) shows a dominant first mode (73% of the total variance) characterized by an oscillating pattern typical of CTWs. The first mode identified with MIOST and CMEMS shows different degrees of similarity with BLUELINK. The degree of variance explained is much less in the altimetry dataset (36% for MIOST, 43% for CMEMS). However, the first spatial EOFs have a correlation of 0.78 (BLUELINK-MIOST) and 0.68 (BLUELINK-CMEMS), while the corresponding principal components have a correlation of 0.53 (BLUELINK-MIOST) and 0.29 (BLUELINK-CMEMS). The improvement of MIOST compared to CMEMS is two-fold: firstly, the spatial EOF of MIOST shows the propagation of the CTWs' amplitudes along the coast better than in CMEMS. Secondly, the principal component of CMEMS identifies fewer CTWs, mostly out of phase compared to MIOST and BLUELINK.

A confirmation of this evaluation can be seen in the evolution over time of the first EOF, which is presented in Figure 7 for ten days during the strongest CTW event observed in the second half of October 2023. MIOST and BLUELINK observe the anticlockwise oscillating amplitude well in phase, except in the first locations (the closest to the Bermagui TG), while the amplitudes of CMEMS are often not consistent with the pattern, as well as out of phase.

## 5 Discussion and conclusion

While gridded sea level maps have often been used in the coastal zone for comparison with tide gauges (e.g., Wöppelmann and Marcos (2016); Oelsmann et al. (2024)), they are usually evaluated as monthly averages or to observe annual, interannual, and long-term trends.

Indeed, Passaro et al. (2023) and Juhl et al. (2024) have shown in the North Sea and in the Patagonian Shelf that the coherence between TGs and daily sea level maps consistently drops for periods below 30 days, which is in agreement with the effective temporal resolution reported by Ballarotta et al. (2019). However, we notice a strong improvement in the correlation of the filtered signal when using the latest version of the CMEMS product (DT2024) compared to the previous one (DT2021, Sanchez-



225



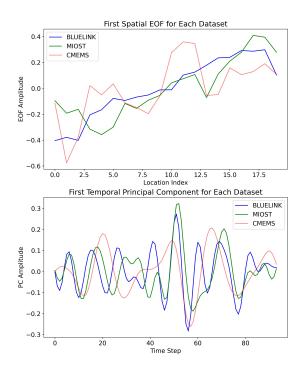


**Figure 6.** Upper plot: Amplitude of the first spatial EOF (above) computed using CMEMS, MIOST and BLUELINK along the equally-spaced coastal points (x-axis). Lower plot: Evolution of the corresponding principal component in time.

Roman et al. (2023)), which still used the optimal interpolation and the same altimetry missions. This can be seen in Figure A1, where we show the results obtained with the same analysis but using DT2021 instead of DT2024. The enhanced capabilities in observing sub-monthly variability are therefore a consequence of two factors: the adoption of a different interpolation scheme based on wavelet transformation and the integration of SWOT data.

The availability of the same interpolation scheme with and without the use of wide-swath altimetry allows us to observe the impact that the latter is having for this particular application. This impact was recently analyzed by Ballarotta et al. (2025), who concluded that the benefits are limited to an improvement of 10 km for the spatial resolution on average. However, their analysis did not consider the improvements in the observation of the temporal scales, and more specifically the coastal zone. Here, we provide the first proof that, at least for shelves wider than 40 km, the combination of the MIOST interpolation with the integration of the wide-swath data is able to detect the CTWs in terms of average phase speed (Figure 5) and spatial pattern (EOF in Figure 6), although the accuracy of the amplitude and phase varies depending on the single event.

This gap in accuracy could be significantly reduced in the next few years with the launch of the Copernicus Sentinel-3 New Generation (S3-NG) Topography mission, which, according to current plans, should consist of two wide-swath altimetry



235

240



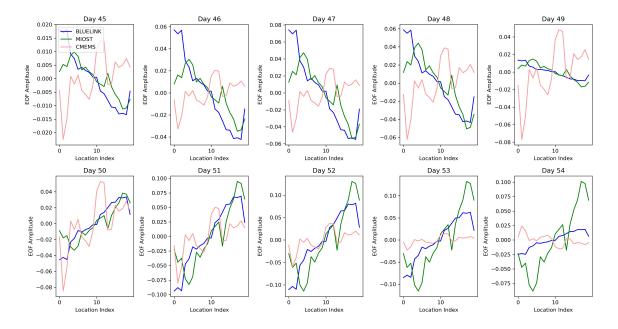


**Figure 7.** Evolution over time of the first EOF for CMEMS, MIOST and BLUELINK, computed for ten days during the strongest CTW event observed in the second half of October 2023.

missions. This would compensate for the disparity between very high spatial resolution and relatively long repeat cycles. The causes of the remaining gap should also be investigated, with a focus on the impact of the Dynamic Atmosphere Correction (DAC, Carrère and Lyard (2003)). This correction is currently applied to the along-track measurements that are then interpolated into the gridded products. Besides the low-frequency static effects due to the inverse barotropic response, it is based on a simulation of the wind-forced barotropic motions by means of the MOG2D-G ocean model for periods shorter than 20 days. The objective of the correction is to remove the signal that would be aliased at lower frequencies on the single along-track records due to their long repeat cycles (never shorter than 10 days). In our region of study, CTWs could also be caused by a direct response of the ocean surface to the changing wind field (Woodham et al., 2013), and therefore their observations could be affected by the application of the DAC.

This study suggests that, especially with the increasing availability of MIOST data during the SWOT era, it is possible to establish an altimetry-based monitoring system for CTWs using filtered time series focused on a set of grid points as "virtual stations." This approach would complement and strengthen studies currently based on sparse in-situ stations (when available) and numerical simulations. Such studies investigate how CTWs control upwelling and productivity in coastal areas, for example, off Peru (Echevin et al., 2014) and in South West Africa (Bachelery et al., 2020), where CTWs account for 70% of the high-frequency variability.





Code and data availability. The complete code used to generate the statistics and plots in this work is publicly available from: https://github.com/ne62rut/coastal\_trapped\_waves

The tide gauge data are an extension of the GESLA dataset (https://www.gesla.org/). They were obtained courtesy of Ivan Haigh (National Oceanography Centre, University of Southampton). The Bluelink Ocean Reanalysis - BRAN2020 (BLUELINK) data were downloaded from in August 2024 from https://geonetwork.nci.org.au/. The CMEMS data is the SEALEVEL\_GLO\_PHY\_L4\_MY\_008\_047 downloaded from https://marine.copernicus.eu/ downloaded first in August 2024 (Version DT2021) and then in February 2025 (Version DT2024). The MIOST data is the "Experimental multimission gridded L4 sea level heights and velocities with SWOT" product available from https://doi.org/10.24400/527896/A01-2024.007, downloaded in July 2024.

## Appendix A: 1D-Validation against tide gauges using DT2021

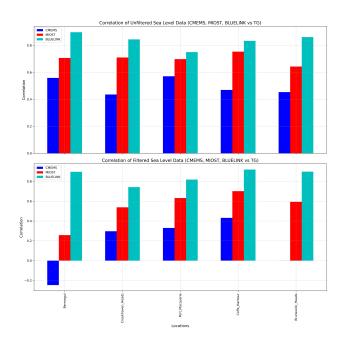


**Figure A1.** Correlation of BLUELINK, CMEMS DT2021 and MIOST time series with the TG data at the closest grid point to each in-situ station. The plot shows the correlation considering unfiltered (upper panel) and filtered (lower panel) time series. CMEMS DT2021 is the previous version of the dataset used Figure A1, which was the standard until November 2024.

#### Appendix B: 2D-Validation against tide gauges





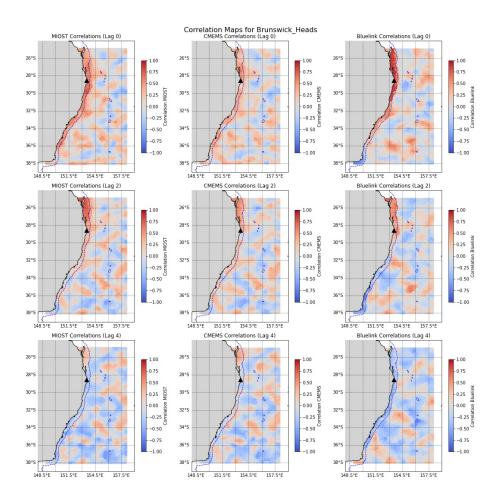


**Figure B1.** Correlation of filtered BLUELINK, CMEMS and MIOST time series at each grid point against the filtered TG data of the station Brunswick\_Heads. Each row corresponds to the lag correlation at day 0, 2, 4. The bathymetry contour of -500m is shown to identify the shelf break.



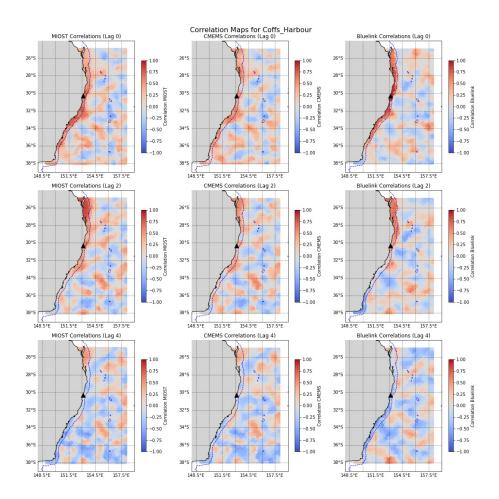


**Figure B2.** Correlation of filtered BLUELINK, CMEMS and MIOST time series at each grid point against the filtered TG data of the station Brunswick\_Heads. Each row corresponds to the lag correlation at day 0, 2, 4. The bathymetry contour of -500m is shown to identify the shelf break.



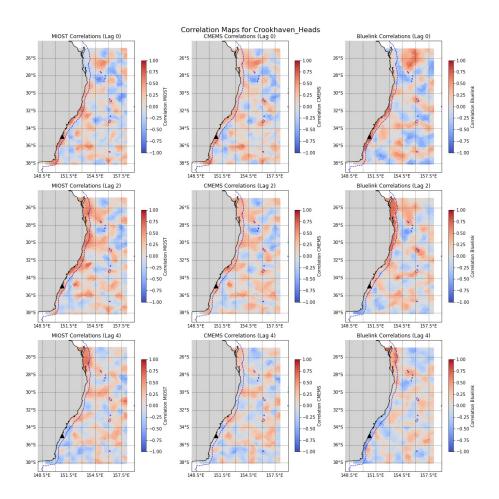


**Figure B3.** Correlation of filtered BLUELINK, CMEMS and MIOST time series at each grid point against the filtered TG data of the station Crookhaven\_Heads. Each row corresponds to the lag correlation at day 0, 2, 4. The bathymetry contour of -500m is shown to identify the shelf break.



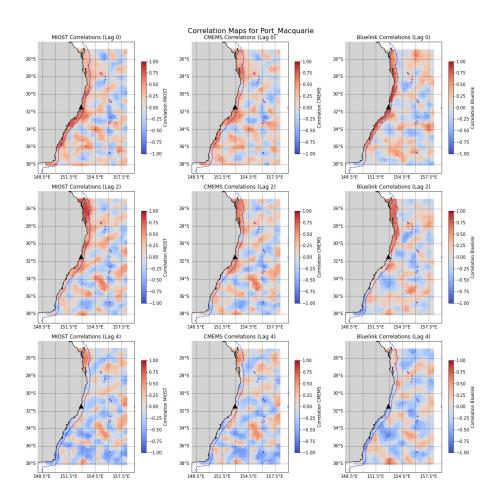


**Figure B4.** Correlation of filtered BLUELINK, CMEMS and MIOST time series at each grid point against the filtered TG data of the station Port\_Macquarie. Each row corresponds to the lag correlation at day 0, 2, 4. The bathymetry contour of -500m is shown to identify the shelf break.





Author contributions. M.P. conducted the research, performed the data analysis, and wrote the manuscript.

Competing interests. No competing interests are present

Acknowledgements. Thanks to Ivan Haigh (National Oceanography Centre, University of Southampton, UK) and Ben Hague (Bureau of Meteorology, Australia) for the help in providing tide gauge data. Thanks to Maxime Ballarotta (Collecte Localisation Satellites, France) for the assistance concerning MIOST.





#### References

- Andersen, O. and Scharroo, R.: Range and Geophysical Corrections in Coastal Regions and Implications for Mean Sea Surface Determination, pp. 103–146, Springer-Verlag, Berlin Heidelberg, 2011.
- Aydın, M. and Beşiktepe, Ş. T.: Mechanism of Generation and Propagation Characteristics of Coastal Trapped Waves in the Black Sea, Ocean Science, 18, 1081–1091, https://doi.org/10.5194/os-18-1081-2022, 2022.
  - Bachelery, M.-L., Illig, S., and Rouault, M.: Interannual Coastal Trapped Waves in the Angola-Benguela Upwelling System and Benguela Nino and Nina events, Journal of Marine Systems, 203, 103 262, https://doi.org/10.1016/j.jmarsys.2019.103262, 2020.
- Ballarotta, M., Ubelmann, C., Pujol, M.-I., Taburet, G., Fournier, F., Legeais, J.-F., Faugère, Y., Delepoulle, A., Chelton, D., Dibarboure, G., et al.: On the resolutions of ocean altimetry maps, Ocean Science, 15, 1091–1109, https://doi.org/https://doi.org/10.5194/os-15-1091-2019, 2019.
  - Ballarotta, M., Ubelmann, C., Bellemin-Laponnaz, V., Le Guillou, F., Meda, G., Anadon, C., Laloue, A., Delepoulle, A., Faugere, Y., Pujol, M.-I., Fablet, R., and Dibarboure, G.: Integrating Wide-Swath Altimetry Data into Level-4 Multi-Mission Maps, Ocean Science, 21, 63–80, https://doi.org/10.5194/os-21-63-2025, 2025.
- Beauchamp, M., Febvre, Q., Georgenthum, H., and Fablet, R.: 4DVarNet-SSH: End-to-End Learning of Variational Interpolation Schemes for Nadir and Wide-Swath Satellite Altimetry, Geoscientific Model Development, 16, 2119–2147, https://doi.org/10.5194/gmd-16-2119-2023, 2023.
  - Carrère, L. and Lyard, F.: Modeling the barotropic response of the global ocean to atmospheric wind and pressure forcing-comparisons with observations, Geophysical Research Letters, 30, 1275, 2003.
- Chamberlain, M. A., Brassington, G. B., OÕDea, E. J., van Sebille, P. J., and Oke, P. R.: Next generation of Bluelink ocean reanalysis with multiscale data assimilation: BRAN2020, Earth System Science Data, 13, 5663–5688, https://doi.org/10.5194/essd-13-5663-2021, 2021.
  - Chelton, D. B., Ries, J. C., Haines, B. J., Fu, L.-L., and Callahan, P. S.: Satellite Altimetry, in: Satellite Altimetry And Earth Sciences: A Handbook Of Techniques And Applications, edited by Fu, L.-L. and Cazenave, A., vol. 69, pp. 1–131, Academic Press, 2001.
- De-Leon, Y. and Paldor, N.: Trapped planetary (Rossby) waves observed in the Indian Ocean by satellite borne altimeters, Ocean Science, 13, 483–494, https://doi.org/10.5194/os-13-483-2017, 2017.
  - Dibarboure, G., Anadon, C., Briol, F., Cadier, E., Chevrier, R., Delepoulle, A., Faugère, Y., Laloue, A., Morrow, R., Picot, N., Prandi, P., Pujol, M.-I., Raynal, M., Trèboutte, A., and Ubelmann, C.: Blending 2D topography images from the Surface Water and Ocean Topography (SWOT) mission into the altimeter constellation with the Level-3 multi-mission Data Unification and Altimeter Combination System (DUACS), Ocean Science, 21, 283–323, https://doi.org/10.5194/os-21-283-2025, 2025.
- Donlon, C. J., Cullen, R., Giulicchi, L., Vuilleumier, P., Francis, C. R., Kuschnerus, M., Simpson, W., Bouridah, A., Caleno, M., Bertoni, R., Rancaño, J., Pourier, E., Hyslop, A., Mulcahy, J., Knockaert, R., Hunter, C., Webb, A., Fornari, M., Vaze, P., Brown, S., Willis, J., Desai, S., Desjonqueres, J. D., Scharroo, R., Martin-Puig, C., Leuliette, E., Egido, A., Smith, W. H. F., Bonnefond, P., Le Gac, S., Picot, N., and Tavernier, G.: The Copernicus Sentinel-6 Mission: Enhanced Continuity of Satellite Sea Level Measurements from Space, Remote Sensing of Environment, 258, 112 395, https://doi.org/10.1016/j.rse.2021.112395, 2021.
- Ducet, N., Le Traon, P.-Y., and Reverdin, G.: Global high-resolution mapping of ocean circulation from TOPEX/Poseidon and ERS-1 and-2, J. Geophys. Res.-Oceans, 105, 19477–19498, 2000.



300

315



- Echevin, V., Albert, A., Levy, M., Graco, M., Aumont, O., Pietri, A., and Garric, G.: Intraseasonal variability of nearshore productivity in the Northern Humboldt Current System: The role of Coastal Trapped Waves, Continental Shelf Research, 73, 14–30, https://doi.org/10.1016/j.csr.2013.11.015, 2014.
- Fu, L.-L., Pavelsky, T., Cretaux, J.-F., Morrow, R., Farrar, J. T., Vaze, P., et al.: The Surface Water and Ocean Topography Mission: A Breakthrough in Radar Remote Sensing of the Ocean and Land Surface Water, Geophysical Research Letters, 51, e2023GL107652, https://doi.org/10.1029/2023GL107652, 2024.
  - Hughes, C., Thompson, K., Minobe, S., Fukumori, I., Griffies, S., Huthnance, J., and Spence, P.: Sea Level and the Role of Coastal-Trapped Waves in Mediating the Interaction Between the Coast and Open Ocean, Surveys in Geophysics, https://doi.org/10.1007/s10712-019-09535-x, 2019.
  - Juhl, M.-C., Passaro, M., Dettmering, D., and Saraceno, M.: Evaluation of the sub-annual Sea Level Anomalies in the continental shelf of the Southwestern Atlantic and their relation to wind variability, Ocean Dynamics, https://doi.org/10.1007/s10236-024-01621-y, 2024.
  - Kemgang Ghomsi, F. E., Raj, R. P., Bonaduce, A., Halo, I., Nyberg, B., Cazenave, A., Rouault, M., and Johannessen, O. M.: Sea Level Variability in Gulf of Guinea from Satellite Altimetry, Scientific Reports, 14, 4759, https://doi.org/10.1038/s41598-024-55170-x, 2024.
- Le Traon, P., Nadal, F., and Ducet, N.: An improved mapping method of multisatellite altimeter data, J. Atmos. Oceanic Tech., 15, 522–534, https://doi.org/https://doi.org/10.1175/1520-0426(1998)015<0522:AIMMOM>2.0.CO;2, 1998.
  - Maiwa, K., Masumoto, Y., and Yamagata, T.: Characteristics of Coastal Trapped Waves along the Southern and Eastern Coasts of Australia, Journal of Oceanography, 66, 243–258, https://doi.org/10.1007/s10872-010-0022-z, 2010.
- Oelsmann, J., Calafat, F. M., Passaro, M., Hughes, C., Richter, K., Piecuch, C., Wise, A., Katsman, C., Dettmering, D., Seitz, 310 F., and Jevrejeva, S.: Coherent Modes of Global Coastal Sea Level Variability, Journal of Geophysical Research: Oceans, 129, https://doi.org/10.1029/2024jc021120, 2024.
  - Passaro, M. and Juhl, M.-C.: On the potential of mapping sea level anomalies from satellite altimetry with Random Forest Regression, Ocean Dynamics, 73, 107–116, https://doi.org/https://doi.org/10.1007/s10236-023-01540-4, 2023.
  - Passaro, M., Schlembach, F., Oelsmann, J., Dettmering, D., and Seitz, F.: Coastal Assessment of Sentinel-6 Altimetry Data during the Tandem Phase with Jason-3, Remote Sensing, 15, 4161, https://doi.org/https://doi.org/10.3390/rs15174161, 2023.
  - Poli, L., Artana, C., and Provost, C.: Topographically Trapped Waves Around South America with Periods Between 40 and 130 Days in a Global Ocean Reanalysis, Journal of Geophysical Research: Oceans, 127, e2021JC018 067, https://doi.org/10.1029/2021JC018067, 2022.
  - Polo, I., Lazar, A., Rodriguez-Fonseca, B., and Arnault, S.: Oceanic Kelvin Waves and Tropical Atlantic Intraseasonal Variability: 1. Kelvin Wave Characterization, Journal of Geophysical Research, 113, C07 009, https://doi.org/10.1029/2007JC004495, 2008.
- Pujol, M.-I., Faugère, Y., Taburet, G., Dupuy, S., Pelloquin, C., Ablain, M., and Picot, N.: DUACS DT2014: the new multi-mission altimeter data set reprocessed over 20 years, Ocean Science, 12, 1067–1090, https://doi.org/https://doi.org/10.5194/os-12-1067-2016, 2016.
  - Sanchez-Roman, A., Pujol, M. I., Faugere, Y., and Pascual, A.: DUACS DT2021 reprocessed altimetry improves Sea Level retrieval in the coastal band of the European Seas, Ocean Science, 19, 793–809, https://doi.org/10.5194/os-19-793-2023, 2023.
- Saraceno, M., Strub, P., and Kosro, P.: Estimates of sea surface height and near-surface alongshore coastal currents from combinations of altimeters and tide gauges, J. Geophys. Res.-Space, 113, C11013, 2008.
  - Schiller, A., Brassington, G. B., Oke, P., Cahill, M., Divakaran, P., Entel, M., and Zhong, A.: Bluelink Ocean Forecasting Australia: 15 Years of Operational Ocean Service Delivery with Societal, Economic and Environmental Benefits, Journal of Operational Oceanography, 13, 1–18, https://doi.org/10.1080/1755876X.2019.1685834, 2019.





- The International Altimetry Team: Altimetry for the Future: Building on 25 Years of Progress, Advances in Space Research, 68, 319–363, https://doi.org/10.1016/j.asr.2021.01.022, 2021.
  - Ubelmann, C., Dibarboure, G., Gaultier, L., Ponte, A., Ardhuin, F., Ballarotta, M., and Faugère, Y.: Reconstructing ocean surface current combining altimetry and future spaceborne Doppler data, Journal of Geophysical Research: Oceans, 126, e2020JC016560, https://doi.org/10.1029/2020JC016560, 2021.
- Ubelmann, C., Carrere, L., Durand, C., Dibarboure, G., Faugère, Y., Ballarotta, M., Briol, F., and Lyard, F.: Simultaneous estimation of ocean mesoscale and coherent internal tide sea surface height signatures from the global altimetry record, Ocean Science, 18, 469–481, https://doi.org/10.5194/os-18-469-2022, 2022.
  - Woodham, R., Brassington, G. B., Robertson, R., and Alves, O.: Propagation Characteristics of Coastally Trapped Waves on the Australian Continental Shelf, Journal of Geophysical Research: Oceans, 118, 4461–4473, https://doi.org/10.1002/jgrc.20317, 2013.
- Woodworth, P., Melet, A., Marcos, M., et al.: Forcing Factors Affecting Sea Level Changes at the Coast, Surveys in Geophysics, 40, 1351–1397, https://doi.org/10.1007/s10712-019-09531-1, 2019.
  - Woodworth, P. L., Hunter, J. R., Marcos, M., Caldwell, P., Menéndez, M., and Haigh, I.: Towards a global higher-frequency sea level dataset, Geoscience Data Journal, 3, 50–59, https://doi.org/10.1002/gdj3.42, 2016.
  - Wöppelmann, G. and Marcos, M.: Vertical land motion as a key to understanding sea level change and variability, Reviews of Geophysics, 54, 64–92, https://doi.org/10.1002/2015RG000502, 2016.